International Journal of Heat and Technology
Vol. 36, No. 3, September, 2018, pp. 1037-1046
Journal homepage: http://iieta.org/Journals/IJHT

Numerical simulation of 3D turbulent bend flow based on unstructured grids

Suiju Lv[1], Feng Gao[2], Chunguang Li[1*]

[1] School of Civil Engineering, North Minzu University, Yinchuan 750021, China
[2] School of General Education, North Minzu University, Yinchuan 750021, China

Corresponding Author Email: cglizd@hotmail.com

https://doi.org/10.18280/ijht.360334

Received: 9 February 2018
Accepted: 12 June 2018

Keywords:
continuous bands, 3D water flow, unstructured grids, finite-volume method, numerical simulation

ABSTRACT

Focusing on the continuous bends in Shapotou section of the Yellow River, this paper probes into the water level variation, planar flow field variation, longitudinal flow variation and secondary flow in the continuous bends. Specifically, a mathematical model for 3D turbulent flow was discretized by the finite-volume method based on unstructured grids, a numerical solution equation was set up under the unstructured grids, and the model was solved by the SIMPLE algorithm using unstructured non-staggered grids. Then, the calculation area was meshed into triangular grids, the grids were densified for the bends, and the vertical direction was divided into multiple layers by the equidistant layering method. The simulated results agree well with the measured value. The convex bank generally had a lower water level than the concave bank. In the first bend, the water level of the concave bank was 0.02m higher than that of the convex bank; in the second bend, the water level of the convex bank was 0.04m higher than the convex bank. The mainstream flow rate was biased towards the concave bank in the continuous bends. With the increase of the central angle in the second bend, the mainstream gradually moved to the convex bank and reached the bank at the tip of the bend. Besides, the surface-bottom vortex on the convex bank became increasingly obvious and intense, the short transition area between the two bends was significantly affected by the high flow rate area of the first bend, and scouring occurred near the convex bank at the inlet and the convex bank at the outlet. These results prove that the proposed model can accurately simulate the 3D bend water flow of natural rivers with complex boundaries; apart from planar spiral flow, the proposed model could simulate the sectional distribution of mainstream flow rate.

1. INTRODUCTION

The law of 3D bend flow has been widely used in various water conservancy projects, namely, river management, port construction, water diversion and sand control and improvement of river navigation [1]. In natural continuous bends, the features of water flow, a focus in river dynamics research, may affect the lateral sediment transport. Therefore, it is very meaningful to identify the exact structure and simulate the accurate features of bend flow in rivers [2]. Currently, 2D and 3D mathematical models of water flow have been extensively applied in fluid computation, because the actual water flows carry lots of 3D features. For instance, Nakamum [3] established a 3D water-sand two-phase flow model to calculate bed surface sediment movement. Pinto [4] used the unstructured grid to create a 3D sediment model under the action of water flow, aiming to disclose the change of non-viscous sediment bed surface. Li Chunguang [5] explores the water flow and sediment transport in Shuidonggou Reservoir using 3D water-sediment model. In general, the effect of numerical simulation mainly depends on the specific calculation method. Among the various calculation methods, the finite volume method is a popular tool for studies on fluid flow and heat transfer, thanks to such advantages of ensuring the local mass conservation of materials, taking up a small storage space, being stable and easy to be extended to 3D situations, and adaptive to complex solution areas. Considering the complex boundaries and irregular solution area of natural rivers, it is difficult to mesh the area into traditional structured grids. As a result, it is imperative to develop numerical solution methods based on unstructured grids that can adapt to complex areas. Below are some of the latest development of these methods. Wang Jinhua [6] relied on 3D unstructured grids to numerically simulate wave-current coupling. Bai Wei [7] calculated the compressive flow field with the SIMPLE algorithm, which is based on unstructured non-staggered grids. Inspired by the eigen-type high-resolution numerical algorithm, Lai Xijun et al. [8] put forward a new 3D unstructured grid hydrodynamic model, and applied the model for numerical simulation of the internal circulation of a closed pool. By classical examples, Lei Guodong et al. [9] verified that the unstructured-grid high-precision finite-volume method can achieve a high resolution of WENO limiter. Yue Zhiyuan et al. [10] established an unsteady 2D flow model of unstructured grids, and successfully simulated the flow motion on complex terrain by the model. Huang Mutao et al. [11] employed non-structural grids to examine the 3D flow field of Donghu Lake in Wuhan, China. With a disordered structure, the unstructured grids are highly flexible in that it is easy to control the size, shape and position of the grids. Hence, these grids are adaptive to the meshing of complex areas. Besides, the nodes can be removed or added at ease when these grids are applied to simulate dynamic boundaries [12-13].

In summary, the traditional discretization formats of the convection term cannot strike a balance between numerical

accuracy and computing efficiency, when unstructured-grid finite-volume method is applied to solve the 3D water flow problem. To overcome the comploutlety of staggered grids, this paper attempts to use the finite-element method with unstructured non-staggered grids, which is based on the SIMPLE algorithm, to solve the flow field control equation.

2. MATHEMATICAL MODEL AND NUMERICAL CALCULATION METHOD

2.1 Mathematical model

In the Cartesian coordinate system, the k-ε turbulent flow mathematical model for 3D unsteady flow can be expressed as:

$$\frac{\partial \phi}{\partial t}+\frac{\partial}{\partial x}(u\phi)+\frac{\partial}{\partial y}(v\phi)+\frac{\partial}{\partial z}(w\phi) = \frac{\partial}{\partial x}(\Gamma_\phi \frac{\partial \phi}{\partial x})+\frac{\partial}{\partial y}(\Gamma_\phi \frac{\partial \phi}{\partial y})+\frac{\partial}{\partial z}(\Gamma_\phi \frac{\partial \phi}{\partial z})+S_\phi \quad (1)$$

where ϕ is a generic variable; t is time; u, v and w are the time-averaged Reynolds flow rates in the x, y and z directions, respectively; Γ_ϕ is the diffusion coefficient; S_ϕ is the source term; v is the viscosity coefficient of water flow; v_t is the eddy viscosity coefficient; ρ is the water density; p is the time-averaged dynamic water pressure; g is the gravity acceleration; k is the turbulent kinetic energy; σ_k is 1.0; G_k is the generated item of turbulent kinetic energy; ε is the dissipation rate of turbulent kinetic energy; σ_ε is 1.2; $C_1=\max\{0.43,\bar{\eta}/(5+\bar{\eta})\}$ with $\bar{\eta}=Sk/\varepsilon$; C_2 is a coefficient with the value of 1.9 [14-15]; S is the average strain rate. The average strain rate can be obtained as $S=\sqrt{2S_{ij}S_{ij}}$, where $S_{ij}=\frac{1}{2}\left(\frac{\partial u_i}{\partial x_j}+\frac{\partial u_j}{\partial x_i}\right)$ (i=1,2,3; j=1,2,3,). Note that u_1, u_2 and u_3 respectively represent u, v and w; x_1, x_2 and x_3 respectively represent x, y and z. Table 1 shows the physical quantities represented by the variables, the diffusion coefficient Γ_ϕ and source term S_ϕ in equation (1).

Table 1. Physical quantities represented by the variables, the diffusion coefficient Γ_ϕ and source term S_ϕ in equation (1).

control equation	ϕ	Γ_ϕ	S_ϕ
Continuity equation	1	0	0
x momentum equation	u	v+v_t	$-\frac{1}{\rho}\frac{\partial p}{\partial x}$
y momentum equation	v	v+v_t	$-\frac{1}{\rho}\frac{\partial p}{\partial y}$
z momentum equation	w	v+v_t	$-\frac{1}{\rho}\frac{\partial p}{\partial z}-g$
k equation	k	$v+\frac{v_t}{\sigma_k}$	G_k-ε
ε equation	ε	$v+\frac{v_t}{\sigma_s}$	$C_1S_\varepsilon-C_2\frac{\varepsilon^2}{k+\sqrt{v\varepsilon}}$

2.2 Control equation discretization

Following the discretization equation (1) of the finite-volume method based on unstructured grids, the control body in the 3D calculation area is a triangular prism and the variables to be obtained are stored at the centre of the control body. As shown in Figure 1, P is the centre of the control body, E is the centre of the adjacent control body, e is the intersection of the control body centreline PE and the control body interface; $n_{1j}=[\Delta y,\Delta x]$ is the normal component of the control body interface, which points to the same direction as line PE if the triangular grids are orthogonal; n_{2j} is the normal component of the control body centreline.

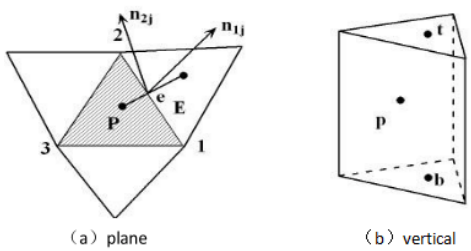

Figure 1. Sketch Map of the control body

As mentioned before, the variables to be obtained are stored at the centre of the control body. Let ΔH be the grid thickness along the z direction. Through the integral operation of the control equation along the control body, we have:

$$\int_{\Delta\Omega}\frac{\partial \phi}{\partial t}d\Omega+\int_{\Delta\Omega}\left(\frac{\partial(u\phi)}{\partial x}\frac{n_x}{|n_{1j}|}+\frac{\partial(v\phi)}{\partial y}\frac{n_y}{|n_{1j}|}+\frac{\partial(w\phi)}{\partial z}\right)d\Omega = \int_{\Delta\Omega}\left[\begin{array}{l}\frac{\partial}{\partial x}(\Gamma_\phi\frac{\partial \phi}{\partial x})\frac{n_x}{|n_{1j}|}+\\ \frac{\partial}{\partial y}(\Gamma_\phi\frac{\partial \phi}{\partial y})\frac{n_y}{|n_{1j}|}+\frac{\partial}{\partial z}(\Gamma_\phi\frac{\partial \phi}{\partial z})\end{array}\right]d\Omega+\int_{\Delta\Omega}S_\phi d\Omega \quad (2)$$

where n_x and n_y are respectively the components of n_{1j} in the x and y directions. It is assumed that, on the control body interface e, the integral variables ϕ, u, v and w are constants equal to the value at the integration points.

Replacing the differential quotient of the instantaneous term with the difference quotient of the time-varying term, we have:

$$\int_{\Delta\Omega}\frac{\partial \phi}{\partial t}d\Omega\doteq\int_{\Delta\Omega}\frac{(\phi_P-\phi_P^0)}{\Delta t}d\Omega=\frac{(\phi_P-\phi_P^0)}{\Delta t}A_{CV}\Delta H \quad (3)$$

where A_{CV} is the area of the control body; ΔH is the thickness of the control body; Δt is the time step.

Using the upwind scheme for the discretization of the convection term, we have:

$$\int_{\Delta\Omega}\left(\frac{\partial(u\phi)}{\partial x}\frac{n_x}{|n_{1j}|}+\frac{\partial(v\phi)}{\partial y}\frac{n_y}{|n_{1j}|}+\frac{\partial(w\phi)}{\partial z}\right)d\Omega$$
$$=\sum_{j=1}^{N_{ED}}\left((u\phi)\Delta y-(v\phi)\Delta x\right)_{ej}\Delta H+\left((w\phi)_t-(w\phi)_b\right)A_{CV}$$
$$=\sum_{j=1}^{N_{ED}}E_{ej}+E_t-E_b \tag{4}$$

where N_{ED} is the number of sides of the control body; $\sum_{j=1}^{N_{ED}}F_{ej}$ is the residual mass flow rate of the inlet and outlet units; $F_{ej}=(u\Delta y\text{-}v\Delta x)_{ej}\Delta H$ is the mass flow rate on the control body interface. If $F_{ej}=(u\Delta y\text{-}v\Delta x)_{ej}\Delta H$ is greater than zero, the mass flows into the control body; if $F_{ej}=(u\Delta y\text{-}v\Delta x)_{ej}\Delta H$ is smaller than zero, the mass flows out of the control body.

$$E_{ej}=\max(F_{ej},0)\phi_P-\max(-F_{ej},0)\phi_E \tag{5}$$

$$E_b=\max(F_b,0)\phi_B-\max(-F_b,0)\phi_P,\quad F_b=w_bA_{CV} \tag{6}$$

$$E_t=\max(F_t,0)\phi_P-\max(-F_t,0)\phi_T,\quad F_t=w_tA_{CV} \tag{7}$$

There are two components of the diffusion term, namely, the orthogonal diffusion term along the normal of line PE (D_j^n) and the cross-diffusion term vertical to line PE (D_j^c). The former can be discretized using second-order precision central difference scheme, while the latter can be determined by the method mentioned in Reference [16]. The discrete form of the diffusion term can be expressed as:

$$\int_{\Delta\Omega}\left[\frac{\partial}{\partial x}(\Gamma_\phi\frac{\partial\phi}{\partial x})\frac{n_x}{|n_{1j}|}+\frac{\partial}{\partial y}(\Gamma_\phi\frac{\partial\phi}{\partial y})\frac{n_y}{|n_{1j}|}+\frac{\partial}{\partial z}(\Gamma_\phi\frac{\partial\phi}{\partial z})\right]d\Omega$$
$$=\sum_{j=1}^{N_{ED}}(\Gamma_\phi)_{ej}\left(\frac{\phi_E-\phi_P}{|d_j|}\frac{d_j\cdot n_{1j}}{|d_j|}-\frac{\phi_{C_2}-\phi_{C_1}}{|l_{1,2}|}\frac{n_{1j}\cdot n_{2j}}{|n_{2j}|}\right)\Delta H \tag{8}$$
$$+\left(\Gamma_\phi\frac{\phi_T-\phi_P}{\Delta H}-\Gamma_\phi\frac{\phi_P-\phi_B}{\Delta H}\right)A_{CV}$$

where d_j is the vector PE; Γ_ϕ is the diffusion coefficient; n_{2j} is the normal of the vector; ϕ_{C1} and ϕ_{C2} are the variable values at nodes 1 and 2, respectively; $l_{1,2}$ is the length of boundary 12. Since the Delaunay triangle is close to an equilateral triangle, the angle between PE and n_{1j} is generally small, indicating that the cross-diffusion term D_j^c is generally smaller than the orthogonal diffusion term D_j^n. As a result, the cross-diffusion term D_j^c was taken as the source term in the calculation process.

The source term S_ϕ is a function of time and physical quantity ϕ. Using the local linearization method, we have the following equation on the control body:

$$\int_{\Delta\Omega}S_\phi d\Omega=\int_{\Delta\Omega}(S_{\phi C}+S_{\phi P}\phi_P)d\Omega$$
$$=(S_{\phi C}+S_{\phi P}\phi_P)A_{CV}\Delta H \tag{9}$$

where $S_{\phi c}$ is the constant part; $S_{\phi P}$ is the variation of S_ϕ at point P along with ϕ.

Substituting equations (3), (4), (8) and (9) into equation (2), we have the full-implicit solution equation:

$$a_P\phi_P=\sum_{j=1}^{N_{ED}}a_{Ej}\phi_{Ej}+a_B\phi_B+a_T\phi_T+b \tag{10}$$

where

$$a_{Ej}=\max(-F_{ej},0)+(\Gamma_\phi)_{ej}\frac{d_j\cdot n_{1j}}{|d_j|^2}\Delta H\quad;$$
$$=\max(F_{ej},0)+(\Gamma_\phi)_{ej}\frac{d_j\cdot n_{1j}}{|d_j|^2}\Delta H-F_{ej}$$
$$a_B=\max(F_b,0)+\Gamma_\phi\frac{A_{CV}}{\Delta H};\quad a_T=\max(-F_t,0)+\Gamma_\phi\frac{A_{CV}}{\Delta H};$$
$$a_P=\sum_{j=1}^{N_{ED}}(a_{Ej}+F_{ej})+(a_B-F_b)+;$$
$$(a_T+F_t)+\frac{A_{CV}\Delta H}{\Delta t}-S_{\phi P}A_{CV}\Delta H$$
$$b=\frac{\Delta HA_{CV}}{\Delta t}\phi_P^0-$$
$$\sum_{j=1}^{N_{ED}}(\Gamma_\phi)_{ej}\frac{\phi_{C_2}-\phi_{C_1}}{|l_{1,2}|}\frac{n_{1j}\cdot n_{2j}}{|n_{2j}|}\Delta H+S_{\phi C}A_{CV}\Delta H$$

where ΔH is the thickness of the control body; A_{CV} is the area of the control body; N_{ED} is the number of sides of the control body; d_j is the vector PE; n_{1j} follows the direction of control body centreline PE; n_{2j} is the normal of vector PE; $l_{1,2}$ is the length of boundary 12; F_{ej}, F_b and F_t are the mass flows on the interfaces, respectively; ϕ_{C1} and ϕ_{C2} are the variable values at nodes 1 and 2, respectively.

2.3 Model solving

For triangular unstructured grids, the computing process may be complicated if the coupling relationship between flow rate and pressure is processed by staggered grids, owing to the special grid shapes and complex grid numbers. Therefore, the SIMPLE algorithm based on unstructured non-staggered grids is generally used to treat the coupling relationship between flow rate and pressure. Here, the solution process uses the momentum difference proposed by Hsu [17] and Rhie [18].

2.4 Initial and boundary conditions

The initial conditions were determined according to the coordinates of the measured section of the river banks, while the smooth boundaries obtained by cubic spline interpolation were taken as the initial boundaries of the river. Through the interpolation of the riverbed elevation, the elevation of each node on the riverbed was obtained and treated as the initial riverbed elevation. Then, the initial water level of the entire river section was computed in turn according to the hydraulic gradient of the measured section. In light of the measured flow rate at the inlet section, it is assumed that the flow rate distribution of the initial flow field is exactly the same as that at the inlet, and the calculated flow rate of the previous period was used as the initial flow rate of the next period. In this way, it takes much less time to stabilize the flow rate. Moreover, initial turbulent kinetic energy k and its initial dissipation rate ε were not set to zero. Otherwise, the program could not start the calculation. The values of these two parameters were empirically determined as 0.01 and 0.001, respectively.

The flow rate at the inlet was determined through measurement. The turbulent energy and its dissipation rate were derived from $k = 0.00375u_{in}^2, \varepsilon = 0.09k^{3/2}$ [19-20], with u_{in} being the average flow rate at the inlet.

The water level at the outlet boundary was also determined by measurement. The flow rate u, turbulent kinetic energy k and its dissipation rate ε were treated according to fully developed conditions:

$$\frac{\partial u}{\partial n} = \frac{\partial v}{\partial n} = \frac{\partial w}{\partial n} = \frac{\partial k}{\partial n} = \frac{\partial \varepsilon}{\partial n} = 0 \tag{11}$$

For free water surface, the water level distribution of the whole field was determined based on the measured water level of each section and the rigid cover assumption, namely:

$$\frac{\partial \phi}{\partial z} = 0, w = 0 \tag{12}$$

where ϕ=u,v,p,k,ε.

3. MODEL VERIFICATION

3.1 Overview of the calculation area

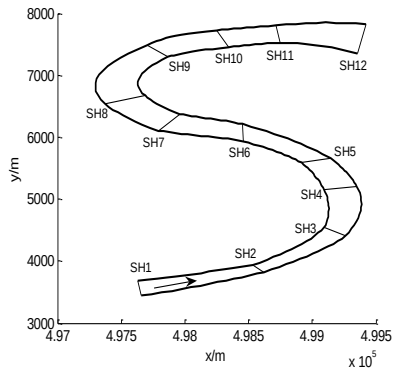

Figure 2. River regime and section distribution

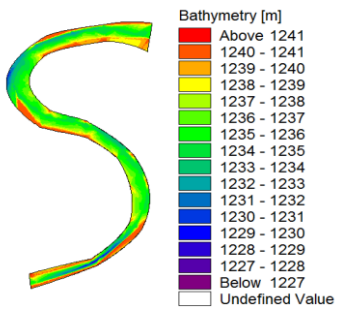

Figure 3. Initial terrain

The Shapotou section of the Yellow River is a typical continuous bending section of natural river. This section exhibits as a continuous curve of two bends with no obvious straight transition in between. The length and average width of the section were 6km and 230.65m, respectively. A total of 12 calculation sections were designed for the simulation area, i.e. SH1~SH12 from the inlet to the outlet. The river regime and section distribution are presented in Figure 2. The initial terrain was determined according to the measurement in December 2008 (Figure 3). The model was verified by the data measured in July 2009. According to the measurement, the upstream water level was 1,240.86m, the downstream water level was 1,240.35m, the average water depth was 4.32m, the average flow rate was 0.57 m/s, and the average water surface slope was 0.17%.

3.2 Grid meshing

The study area was meshed into unstructured triangular grids. The grids in the bends were densified. After the densification, the size of triangular grids fell between 300m^2 and 50m^2. Fifteen layers of grids were arranged in the vertical direction (Figure 4).

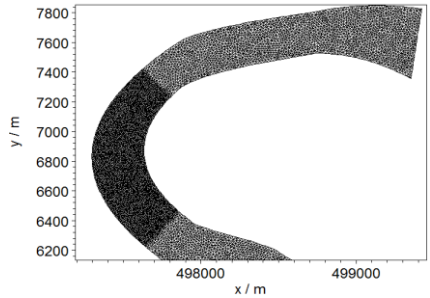

(a) Grid layout of SH6~SH10

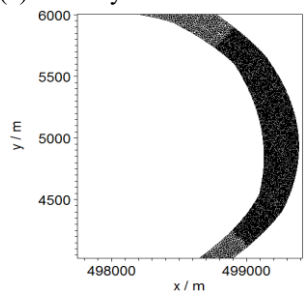

(b) Grid layout of SH2~SH5

Figure 4. Grid layout of the calculation area

3.3 Analysis of calculation results

3.3.1 analysis of water level calculation results

Table 2. Calculated and measured water levels (unit: m)

section	Calculated water levels	Measured water levels	error
SH1	1240.88	1240.86	0.02
SH2	1240.86	1240.85	0.01
SH3	1240.81	1240.84	-0.03
SH4	1240.64	1240.68	-0.04
SH5	1240.64	1240.68	-0.04
SH6	1240.65	1240.69	-0.04
SH7	1240.60	1240.65	-0.05
SH8	1240.52	1240.57	-0.05
SH9	1240.48	1240.51	-0.03
SH10	1240.44	1240.43	0.01
SH11	1240.38	1240.35	0.03
SH12	1240.33	1240.35	-0.02

Before simulation, the inlet flow rate was set to 833.73m^3/s,thee inlet water level to 1240.85m and the outlet water level to 1,240.35m. Table 2 compares the calculated water level and the measured water level. It is clear that the two values agree well with each other. Figure 5 provides the trend of water level change in the study area. As shown in the figure, the water level gradually decreased along the flowing direction; the water in the bends were subjected to the centrifugal force, leading to a lateral slope: the water level

close to the concave bank was higher than that close to the convex bank. In the first bend SH2~SH5, the water level near the convex bank was 1,240.62m, 0.02m lower than that near the concave bank (1,240.64m). In the second bend SH7~SH9, the water level near the convex bank was 1,240.48m, 0.04m lower than that near the concave bank (1,240.52m).

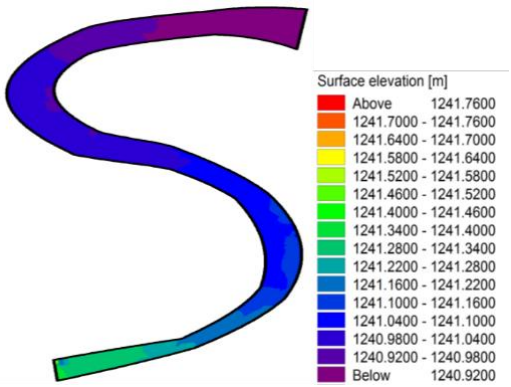

Figure 5. Trend of water level change

3.3.2 Analysis of calculation results on plane flow field

Under the influence of the transition section, the mainstream of the bend flow was not consistent with the centreline of the bends. Figures 6 and 7 respectively shows the distribution of calculated and measured flow rates. Figure 8 compares the calculated flow rate with measured flow rate in typical sections SH3 and SH7.

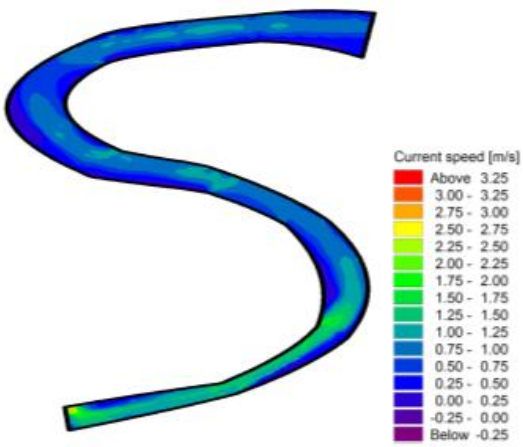

Figure 6. Distribution of calculated flow field

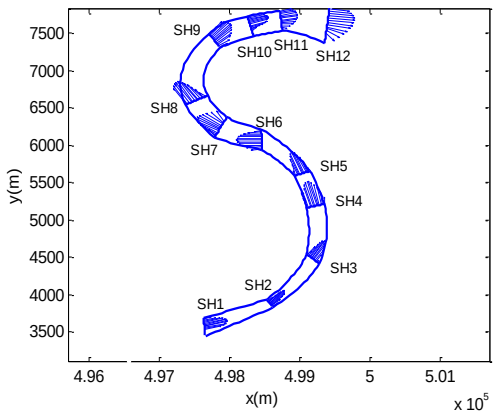

Figure 7. Distribution of measured flow field

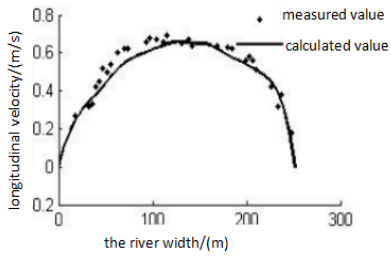

(a) SH3

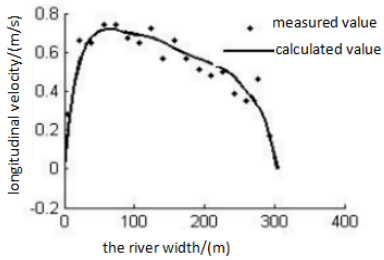

(b) SH7

Figure 8. Comparison between calculated and measured flow rates

According to the calculated and measured results, the mainstream was biased towards the concave tank in the first bend and started to move back towards the centreline in the transition section. The residual circumfluence from the first bend at the inlet of the second bend pushed the fast-moving surface water towards the convex bank. With the increase of the central angle of the second bend, the influence of the reverse circumfluence gradually decreased. Thus, the mainstream gradually shifted towards the concave bank, and was completely biased towards the concave bank when it reached the tip of the bend. These phenomena reveal that the weakening of the circumfluence depends on the length of the transition section, and that the scouring mainly occurs near the convex bank of the inlet and the concave bank of the outlet.

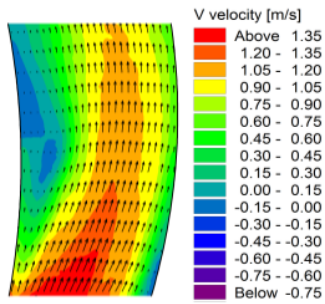

(a) Surface flow rate distribution

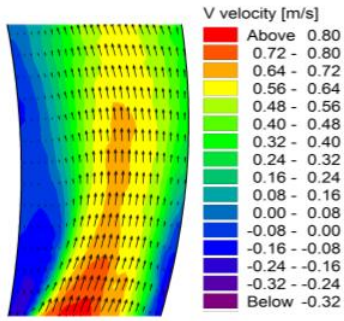

(b) Bottom flow rate distribution

Figure 9. Surface and bottom flow rate distributions in the first bend

Figure 9 shows the flow rate distribution on the surface and bottom of the first bend. It can be seen that the surface flow was biased to the concave bank while the bottom flow was biased to the convex bank, and that the surface-bottom vortex on the convex bank became increasingly obvious and intense.

Figure 10 shows the flow rate distribution on the surface and bottom of the first bend. It can be seen that the flow rate distribution carried the features of the curved water flow: the surface flow was biased to the concave bank while the bottom flow was biased to the convex bank, forming an obvious backflow on the convex bank.

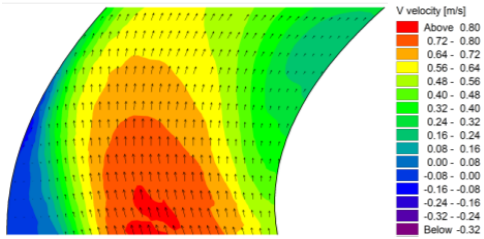

(a) Surface flow rate distribution

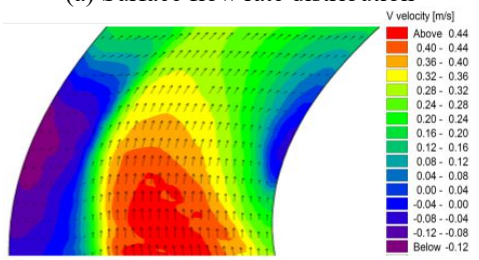

(b) Bottom flow rate distribution

Figure 10. Surface and bottom flow rate distributions in the second bend

3.3.3 Vertical distribution of longitudinal flow rate

Figure 11 is the contour map of the measured and calculated flow rates at 10 typical sections (SH2~SH11) of the continuous bends of Shapotou river section (unit: m/s).

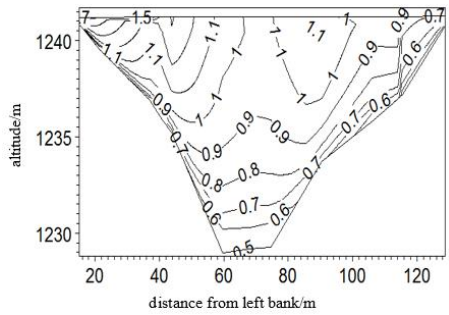

(a1) Calculated flow rate of section SH2

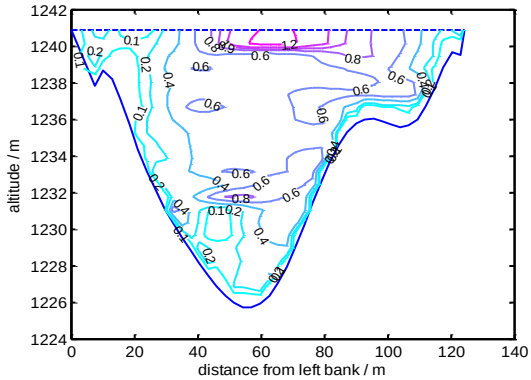

(a2) Measure flow rate of section SH2

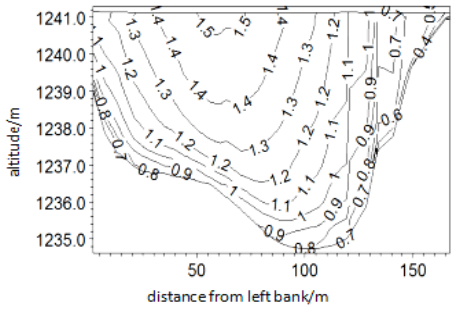

(b1) Calculated flow rate of section SH3

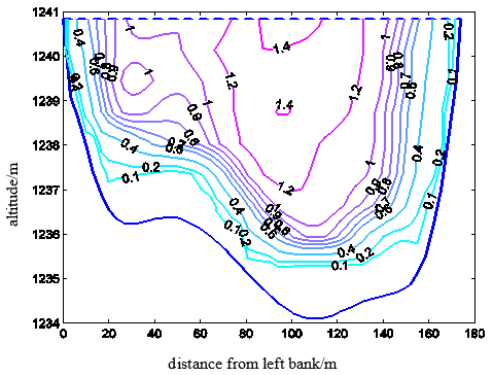

(b2) Measure flow rate of section SH3

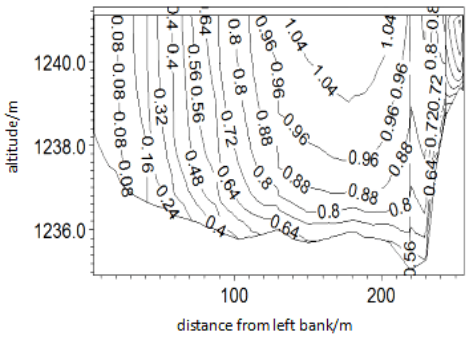

(c1) Calculated flow rate of section SH4

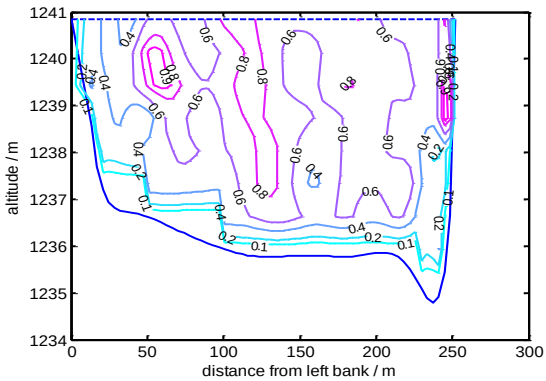

(c2) Measure flow rate of section SH4

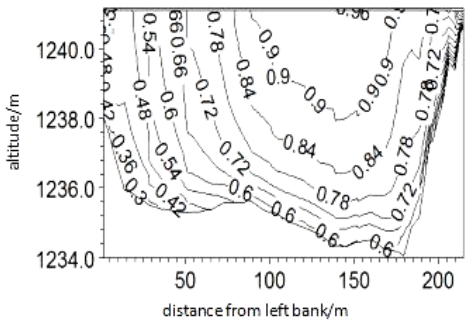

(d1) Calculated flow rate of section SH5

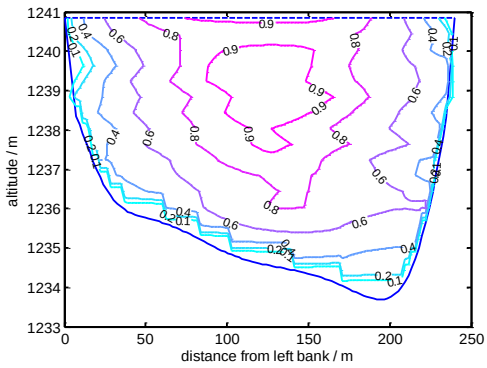

(d2) Measure flow rate of section SH5

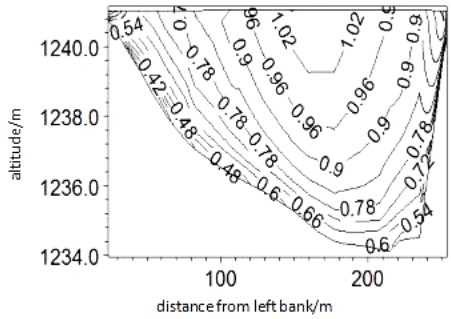

(e1) Calculated flow rate of section SH6

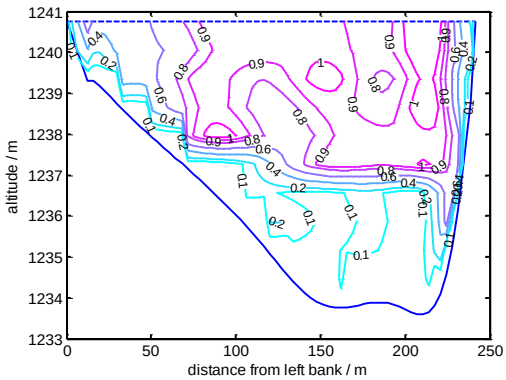

(e2) Measure flow rate of section SH6

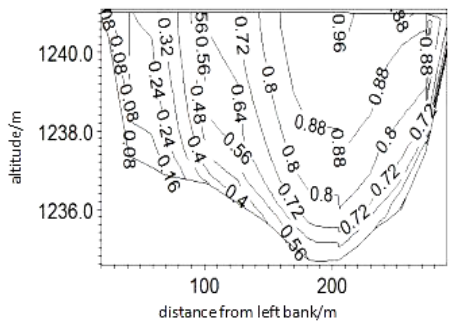

(f1) Calculated flow rate of section SH7

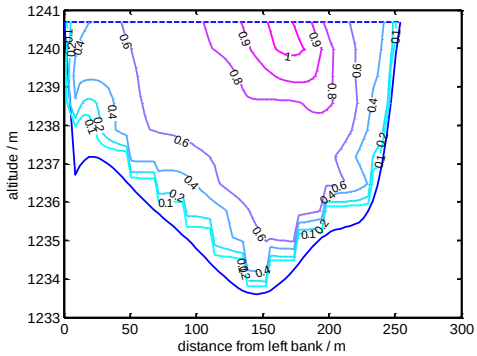

(f2) Measure flow rate of section SH7

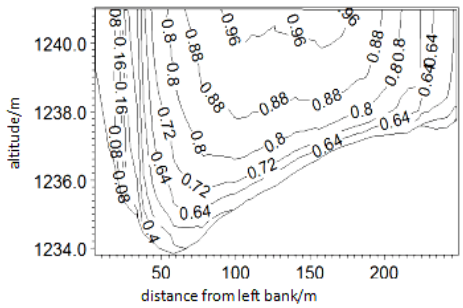

(g1) Calculated flow rate of section SH8

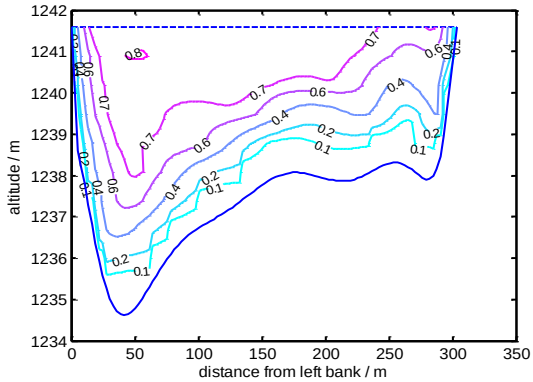

(g2) Measure flow rate of section SH8

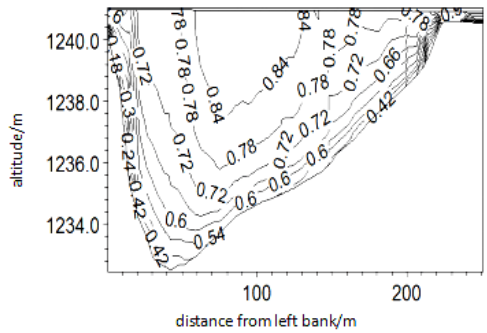

(h1) Calculated flow rate of section SH9

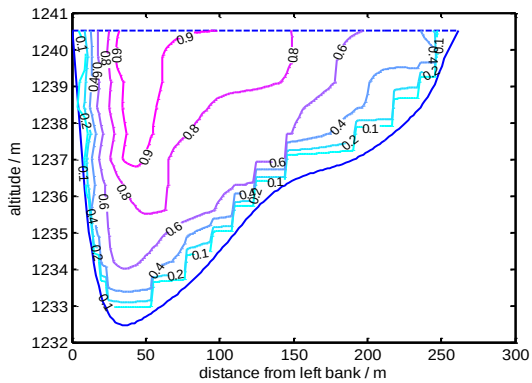

(h2) Measure flow rate of section SH9

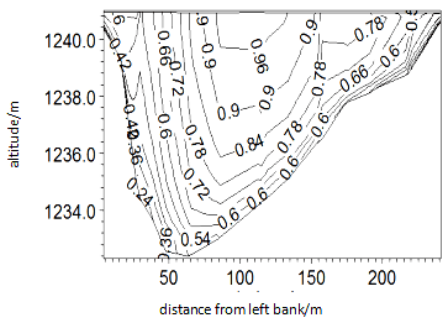

(i1) Calculated flow rate of section SH10

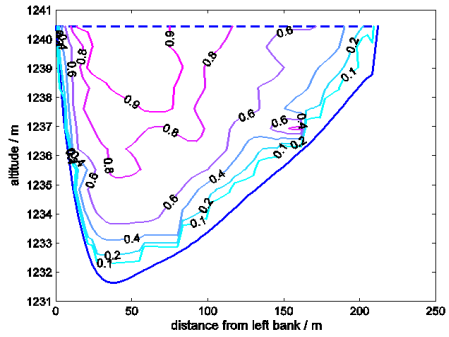

(i2) Measure flow rate of section SH10

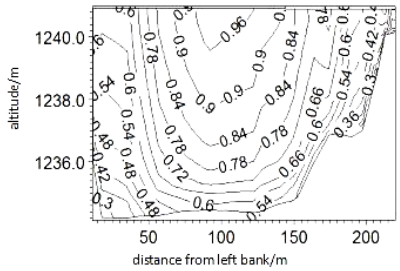

(j1) Calculated flow rate of section SH11

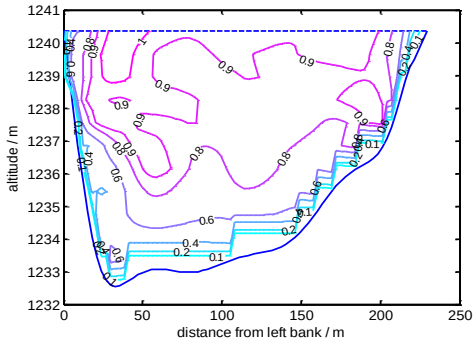

(j2) Measure flow rate of section SH11

Figure 11. Contour map of the measured and calculated flow rates at 10 typical sections

The contour map reveals that, despite many similarities, the calculated distribution of surface and bottom flow rates were quite different from those measured on site. The difference is mainly attributable to two factors: First, the measurement devices were partially affected by the complex field environment and the rapid and turbulent flows of the Yellow River; Second, the section data extracted from the simulation can approximate but not coincide with the measured data. In section SH2, which lies at the inlet of the first bend, the flow rate was basically uniformly distributed and the high rate area appeared at the centre of the river. These features are resulted from the impacts of the shape of upstream channel. In section SH3, which lies at the tip of the bend, the high flow rate area shifted towards to concave bank (right bank). The shift was completed in section SH5. The transition section SH6 was so short that the high flow rate area of the first bend still had a great influence. Although the high flow rate area was on the concave bank (right bank), the area started to move towards the convex bank in SH6. In section SH7, which lies at the inlet of the second bend, the high flow rate area appeared on the concave bank (right bank), and then gradually moved towards the convex bank (left bank). The movement was completed in SH8 and SH8. After leaving the bends, the high flow rate area began to return to the middle in SH10 and SH11.

Figure 12 compares the calculated and measured flow rates on 5 vertical lines of 8 typical sections of the continuous bends, where y is the distance to the left bank, the abscissa u is the mainstream flow rate, the ordinate is the water level, the solid line is the calculated value and * is the measured value.

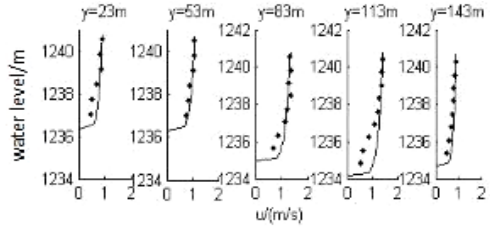

(a) SH2

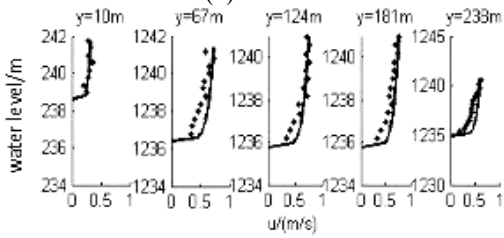

(b) SH3

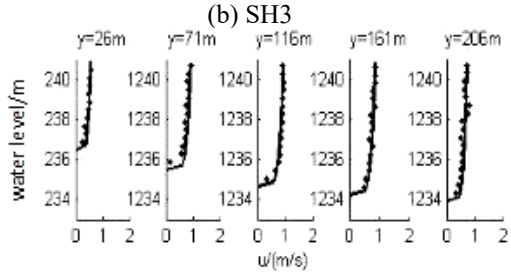

(c) SH4

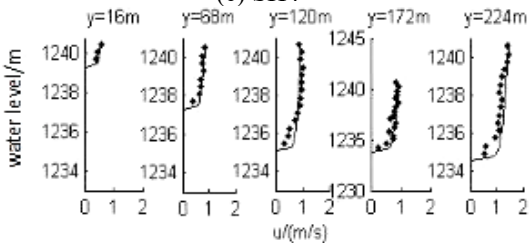

(d) SH5

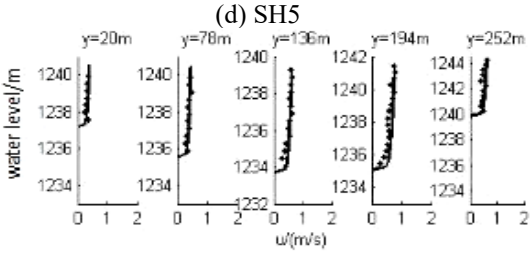

(e) SH6

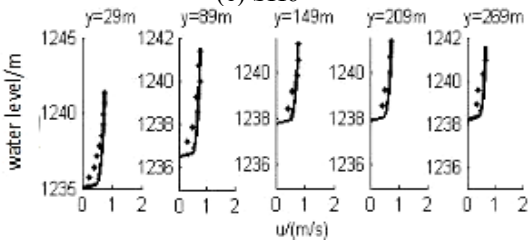

(f) SH7

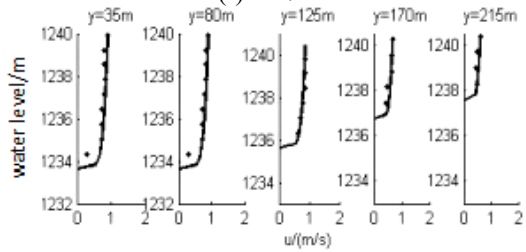

(g) SH8

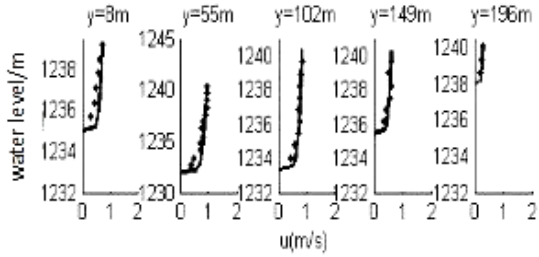

(h) SH9

Figure 12. Calculated and measured flow rates on 5 vertical lines of 8 typical sections

It can be seen from the figure that the calculation results were close to the measured results, both of which demonstrate the distribution law of water flow in continuous bends. Along the vertical direction, the mainstream flow rate basically followed the logarithmic law. The flow rate gradient was large near the riverbed and changed little far from the riverbed.

4. CONCLUSIONS

This paper establishes a numerical model for 3D turbulent flow based on unstructured grid, discretizes the control equations through unstructured-grid finite-volume method, and solve the model using the SIMPLE algorithm of the unstructured non-staggered grids. The proposed model was applied to numerically simulate the continuous bends in Shapotou section of the Yellow River. Through the simulation, the author obtained the results on the distribution of the planar flow field, the vertical distribution of the longitudinal flow rate, and the lateral flow rate (secondary flow). The simulated results agree well with the measured data, revealing that the model can accurately simulate the bend water flow of natural rivers with complex boundaries and the water flow patterns in all directions. Apart from planar spiral flow, the proposed model could simulate the sectional distribution of mainstream flow rate. Thus, our 3D turbulent flow is a desirable simulation tool for the motion law of water in natural rivers. The research findings lay a solid basis for the research into the riverbed variation and water quality in the study area.

ACKNOWLEDGMENT

This paper is supported by the National Science Foundation of China (Grant No. 11761005); The Ningxia Natural Science Foundation (Grant No. 2018AAC03115).

REFERENCE

[1] Song ZY. (2003). Generality of the Rozovskii's formulas on circulation at river bends. Advances in Water Science 14(2): 218-221. https://doi.org/10.3321/j.issn:1001-6791.2003.02.018

[2] Lv SJ, Feng MQ, Li CG. (2013). 3-D numerical simulation of flow in natural meandering channel. Hydro-Science and Engineering (5): 10-16. https://doi.org/10.3969/j.issn.1009-640X.2013.05.002

[3] Nakamura T, Yim SC. (2011). A nonlinear Three-dimensionl coupled Fluid-Sediment interaction model for large seabed deformation. Journal of Offshore Mechanics and Arctic Engineering-Transactions of the ASME 133(3): 1-14. https://doi.org/10.1115/1.4002733

[4] Pinto L, Fortunato AB, Zhang Y, Oliveira A, Sancho FEP. (2012). Development and validation of a three-dimensional morphodynamic modelling system for non-cohesive sediment. Ocean Modelling 57-58: 1-14. https://doi.org/10.1016/j.ocemod.2012.08.005

[5] Li CG, Yang C. (2013). Numerical simulation of three dimensional flow and sediment transport in ningxia shuidonggou reservoir. China Rural Water and Hydropower 12: 45-50. https://doi.org/10.3969/j.issn.1007-2284.2013.12.012

[6] Wang JH. (2011). Establishment and application of three-dimensional nonstructural wave and current coupling numerical model. PHD Thesis of Dalian University of Technology.

[7] Bai W, E XQ. (2003). Implement of SIMPLE algorithm based on unstructured colocated meshes. Chinese Journal of Computational Mechanics 20: 702-710. https://doi.org/10.3969/j.issn.1007-4708.2003.06.010

[8] Lai XJ, Qu ZJ, Zhou J, Shen MB. (2006). 3-D hydrodynamic model for shallow water on unstructured grids. Advances in Water Science 17(5): 693-699.

[9] Lei GD, Li WA, Ren YX. (2011). High-order unstructured-grid WENO FVM for compressible flow computation. Chinese Journal of Computational Physics 28(5): 633-640.

[10] Yue ZY, Cao ZX, Li YW. (2011). Unstructured grid finite volume model for two-dimensional shallow water flows. Chinese Journal of Hydrodynamics 26(3): 359-367. https://doi.org/10.3969/j.issn1000-4874.2010.03.013

[11] Huang MT, Tian Y. (2014). Three-dimensional lake hydrodynamic numerical modeling and its application to Lake Donghu. Chinese Journal of Hydrodynamics 29(1): 114-124. https://doi.org/10.3969/j.issn1000-4874.2014.01.015

[12] Aguizir A, Zantalla E, Ait Yassne Y, Selhaoui N, Bouirden L. (2016). Influence of the concentration of tellurium in tlie hardening mechanism of the lead-tellurium alloys for battery grids. Annales de Chimie: Science des Materiaux 40(3-4): 121-129

[13] Du M. (2005). Unstructured mesh generation and its application in 2D hydrodynamic model. Master Thesis of Tianjin University. https://doi.org/10.7666/d.y849139

[14] Shmitt FG. (2007). Direct test of a nonlinear constitutive equation for simple turbulent shear flows using DNS data. Comp-utation in Nonlinear Science and Numerical Simulation 12(7): 1251-1264. https://doi.org/10.1016/j.cnsns.2006.01.015

[15] Tao WQ. (1995). Numerical heat transfer. Xi'an: Xi'an Jiao Tong University Press.

[16] Olaiju OA, Hoe YS, Ogunbode EB. (2018). Finite element and finite difference numerical simulation comparison for air pollution emission control to attain cleaner environment. Chemical Engineering Transactions 63: 679-684. https://doi.org/10.3303/CET1863114

[17] Hsu C. (1981) A curvilinear-coordinate method for momentum, heat and mass transfer of irregular geometry. Ph D thesis, University of Minnesota.

[18] Rhie CM, Chow WL. (1983). A numerical study of the turbulent flow past an isolated airfoil with trailing edge separation. 3rd Joint Thermophysics, Fluids, Plasma and

Heat Transfer Conference 21: 1525-1552. https://doi.org/10.2514/6.1982-998
[19] Liu SH, Zhao SL, Luo QS. (2007). Simulation of low concentration sediment-laden flow based on two-phase flow theory II—Solution and verification. Journal of Wuhan University 4(4): 5-8. https://doi.org/10.3969/j.issn.1671-844.2007.04.002
[20] Li Y, Lv H. (2018). Numerical simulation of mass transfer of slug flow in microchannel. Chemical Engineering Transactions 65: 325-330. https://doi.org/10.3303/CET1865055